Final Report- External Grant Award No. 06HQGR0137

Seismotectonics of the New Madrid Seismic Zone: New Data and Improved Analytical Techniques

Stephen Horton
Center for Earthquake Research and Information, University of Memphis
3890 Central Avenue
Memphis, TN 38152
Telephone: (901) 678-4896
FAX: (901) 678-4734
Email: shorton@memphis.edu

Start Date: January 1, 2006
End Date: March 31, 2009

Abstract
The Cooperative New Madrid Seismic Network (CNMSN) prior to 1998 was composed mostly of single component (vertical) short-period seismometers, and so did not provide reliable S-wave arrival times (due to converted phases) and no S-wave polarity information. An upgrade of the network beginning in 1998 included deployment of 96 three-component stations and the installation of 13 broadband seismometers. We performed two analyses of the newly available data.

First we performed high-resolution earthquake locations for the New Madrid seismic zone (NMSZ) using the double-difference location method. The NMSZ consists of four major arms of seismicity centered in the central United States and is one of the few places of concentrated earthquake activity far from a major plate boundary. The zone generates approximately 200 earthquakes per year. Double-difference relocation techniques proved well suited for this region because the distance between neighboring events is small and station coverage is relatively dense. The initial data set consisted of 1,394 earthquakes recorded between 2000 and 2006 by 197 stations. The catalog contained approximately 67,000 P-wave and 54,000 S-wave observations, which yields 480,000 differential times. Waveform cross-correlation of P and S waves provides an additional 135,000 high precision differential times. Relocated hypocenters align along individual segments of the seismic zone, providing a sharper image of the NMSZ faults. Results were reported in the Seismological Research Letters by Dunn et al. (2010) and at two professional meetings; Dunn et al. (2007a, 2007b).

For the second analysis, P- and SH- wave polarity from data recorded by the CNMSN between 2000-2007 are used to determine 290 focal mechanisms. Two main trends of strike-slip nodal planes match seismicity or structures in the northern Mississippi Embayment. Nodal planes oriented ~50° are parallel to the Reelfoot Rift. Nodal planes oriented ~30° are parallel to the Northern Arm and the Mississippi Embayment axis. Two major trends of reverse faults occur in the Central Segment. One is oriented about 147° and is parallel to the average trend of seismicity in that segment. The other is oriented north-south. This trend is anticipated for reverse faults secondary to through going strike-slip faults oriented about 45° such as the Blytheville fault zone. Normal faults concentrate in the Central Segment and show a variety of nodal plane orientations. An inversion for regional stress field shows a horizontal maximum compressive stress oriented 79º ±30°. This work formed the basis of the Masters of earth science thesis for Greg Johnson (2008). The results have been presented at two professional meetings; Johnson et al. (2008) and Horton and Johnson (2010). Greg and I are currently creating a manuscript for BSSA.

Project Results
We performed two analyses on newly available high quality 3 component recordings of earthquakes in the NMSZ.

Part 1: High-resolution Earthquake Relocation in the New Madrid Seismic Zone

INTRODUCTION

The New Madrid seismic zone (NMSZ) (Figure 1) is located in the central United States and is the most seismically active region east of the Rocky Mountains. Three significant large (magnitude greater than 7) earthquakes occurred in this region in 1811 and 1812. These earthquakes are some of the largest to have occurred in the central and eastern United States, and paleoseismology indicates that earthquakes of comparable size occurred in A.D. 900 and 1450 (Johnston and Schweig, 1996). The seismic zone is thought to be due to reactivation of structures associated with the Cambrian-age Reelfoot ri$(Ervin and McGinnis 1975; Hildenbrand and Hendricks, 1995). Dextral slip on NE-trending faults and reverse slip on NW-trending faults within the NMSZ is consistent with the present regional stress field, with the maximum compression axis oriented between 70 and 80° (Ellis 1994; Grana and Richardson 1996; Johnson 2008). Why the NMSZ generates high levels of microseismicity, while other ancient fault systems that are also optimally oriented within the present-day stress field do not, remains an open question (Liu et al. 1992; Pollitz et al. 2001; Forte et al. 2007).

The Reelfoot rift is located within the Mississippi embayment (Figure 1), a coastal plain– related basin with an unconsolidated sediment cover averaging about 600 m in the study area. The margins of the Reelfoot rift are defined by several steeply dipping normal faults (Nelson and Zhang 1991; Parrish and VanArsdale 2004) and associated mafic intrusions (Hildenbrand and Hendricks 1995). Paleozoic sediments ranging from Cambrian to Middle Ordovician age lie below the unconsolidated sediments and above crystalline basement rock (Howe and Thompson 1985). Basement rock is probably the Eastern Granite Rhyolite Province. This province consists primarily of granite, granite porphyry, and dioritic gneiss (Bickford et al. 1986; Csontos and VanArsdale 2008).

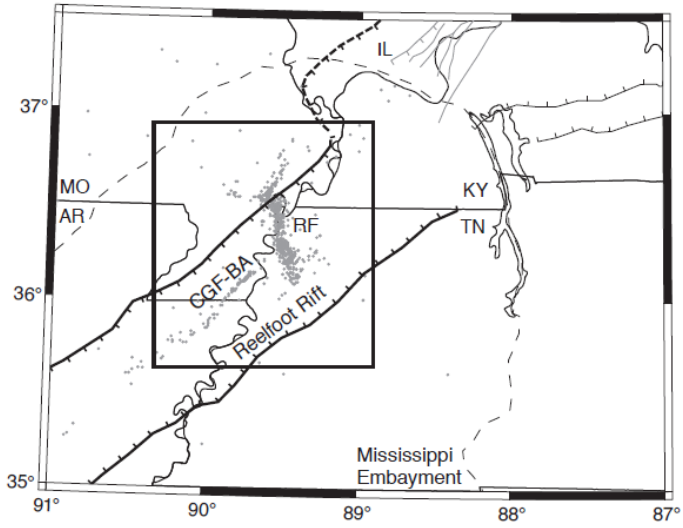

Figure 1. Tectonic setting of the New Madrid seismic zone showing the Mississippi embayment and the Reelfoot rift. Mississippi embayment outlined by the dashed line. NMSZ is outlined by a box. Gray dots indicate earthquakes occurring between 2000 and 2006. CGF-BA is Cottonwood Grove fault- Blytheville arch. RF is Reelfoot arch.

Previous refraction studies in the NMSZ provide a good indication of the 1D velocity structure of the upper portion of the crust (Mooney et al. 1983; Catchings 1999). Mooney et al. (1983) propose a model of the Mississippi embayment consisting of six layers including a low-velocity, unconsolidated sediment layer at the surface and a 3–5-km-thick layer of Paleozoic sedimentary rocks. The Paleozoic rock sequence has relatively fast seismic wave velocity at the top and slow velocity at the bottom. This suggests the presence of a low-velocity layer at depth. Underlying this is crystalline basement with an average crustal thickness of 41km. The 1D velocity model used in this study (Chiu et al. 1992) is based, in part, on the refraction study of Mooney et al. (1983) and contains a 600-m-thick low-velocity surface layer and a low-velocity layer at approximately 3–5 km depth.

Microseismicity within the NMSZ occurs along four distinct lineaments (Figures 1 and 2). We divide the seismicity into six clusters for the purposes of this study. The Cotton wood Grove fault–Blytheville Arch segment (CGF-BA) extends in a NE–SW orientation along the central Reelfoot rift. This segment is broken into clusters 1 and 2 (Figure 2). Motion along this segment and the northeastern band of seismicity (cluster 4) is predominately dextral strike-slip. The Reelfoot fault (RF) extends NW–SE across the Mississippi River and produces most of the microseismicity recorded within the NMSZ. The RF is divided into clusters 5 and 6 (Figure 2). RF focal mechanisms show a dominance of reverse faulting with numerous normal and strike-slip mechanisms (Johnson 2008). We assign the smaller, northwestern segment of earthquakes to cluster 3 (Figure 2).

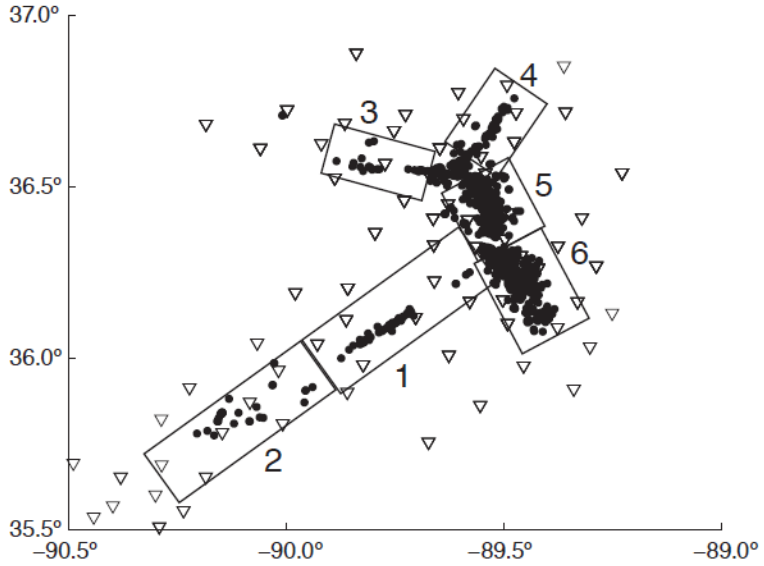

Figure 2. Map of the NMSZ showing the division of seismicity into clusters. Triangles are stations, gray circles indicate earthquake epicenters. Clusters are denoted by large boxes and are numbered for reference.

Catalog locations derived using 1D velocity models within the NMSZ provide a broad picture of active seismogenic faults but have formal errors on the order of 0.5–2 km. Microseismicity collected as part of the 1989–91 Portable Array for Numerical Data Acquisition (PANDA) deployment (Chiu et al. 1992) and relative relocations using the joint hypocenter determination

(JHD) technique (Pujol et al. 1997; Mueller and Pujol 2001) provide a sharper picture of the ac tive NMSZ fault structures, especially as a function of depth. Recent upgrades to the Cooperative New Madrid Seismic Network (CNMSN) provide a new data set of high quality P and S arrivals for local earthquakes, which we analyze in this study. We apply the double-difference (DD) relative earth quake location program hypoDD to this new data set and produce high-resolution images of faulting within the NSMZ. The DD technique minimizes errors due to unmodeled velocity struc ture much like JHD techniques, but it also reduces intraevent location error by utilizing high-accuracydifferential times derived from catalog picks and via waveform cross-correlation (WCC) (Waldhauser and Ellsworth 2000).

DATA

The data set consists of P- and S-wave arrival times from 1,394 earthquakes that occurred in the region between 2000 and 2006. All data were obtained from the CNMSN catalog. S-wave onsets in the NMSZ are difficult to identify due to S-to-P-wave conversions at the Paleozoic rock–unconsolidated sediments interface and, therefore, only arrivals recorded at three-component stations are used. A total of 313 stations are used, with most of the phases recorded at 197 stations.

Initial catalog earthquake locations are determined using the program HYPOELLIPSE (Lahr 1980). Most earthquakes occur along the four arms of seismicity previously described (Chiu et al. 1992; Pujol et al. 1997). Events are required to have a minimum of eight P-wave arrivals for inclusion in the relocation study. The 1D velocity model used in the catalog locations as well as in the DD relocations is the model developed for the NMSZ (Chiu et al. 1992). Ultimately, 283,331 P-wave catalog and 195,578 S -wave catalog di!erential times are used in the earthquake relocations. The data set includes 81,709 P-wave WCC and 53,541 S-wave WCC differential travel times. A total of 614,159 differential times are used in the relocations.

METHOD

The program hypoDD is used to compute earthquake relocations (Waldhauser 2001). This program minimizes errors introduced to earthquake locations by unmodeled two- or three-dimensional velocity structure by assuming that the spatial separation between hypocenters is small compared to the hypocenter-station distance, and therefore velocity variation is the same along event-pair raypaths. The DD algorithm, therefore, requires the establishment of a network of differential times for closely spaced event pairs (Waldhauser 2001). The closer two hypocenters are to one another and the more recording stations they have in common, the stronger the event-pair link. Note that two events that are close spatially may not constitute a strong link if they do not have arrivals at common stations. Seismicity is dense within the NMSZ and station coverage is almost constant since 2000, creating many strong event pairs. Events are linked using a nearest-neighbor approach that is governed by the number of observed arrival times for each pair at common stations and by search radius (Waldhauser 2001). Each event pair must be within five kilometers and have a minimum of eight P- and S-wave arrivals at common stations to be included in the NMSZ study. Relative locations are found by minimizing the residual differences between observed and calculated travel times for sets of closely located events (Waldhauser 2001). WCC improves the relocations by providing more accurate P and S differential times, thus reducing error due to inaccurate, analyst-derived onset times. The method of WCC used in this study calculates the lag time between two waveforms corresponding to the

largest peak of the cross-correlation function in the time domain (Horton et al. 2005). A minimum correlation coefficient threshold of 0.7 is required for inclusion in the data set.

We refine the resultant set of differential times is by applying residual and distance weighting during the inversion. Residual weighting is used to downweight phases above a certain residual threshold, set to 0.4 to 0.5 milliseconds in this study. Distance weighting is used to downweight event pairs with interevent distances greater than a defined distance; we use 3 km for the central RF segment and 4 km for all other faults. the residual weighting factor is determined by comparing residuals for the data set. A majority have residuals within 0.5 milliseconds. These weighting factors ensure that only the highest quality data are used in the inversion.

HypoDD employs a hierarchical weighting scheme allowing P-wave and S-wave WCC and catalog differential times to be weighted independently for each iteration. Different weighting schemes are tested, and the final weighting scheme for the cross-correlation (CC) and catalog (CT) differential times is shown in Table 1. The initial iterations weight the P and S-waveform CC data less than the CT data, and, gradually, the CT data are downweighted in favor of the CC data. The first iterations weight the CT differential times higher to allow for relocation on a rough scale. The CC differential times are upweighted to allow relocation at a finer scale.

TABLE 1
Weighting Values

Iteration	CC P wave weight	CC S wave weight	CT P wave weight	CT S wave weight
1–2	0.01	0.008	1.0	0.8
3–7	1.0	0.8	1.0	0.8
8–12	1.0	0.8	0.01	0.008

Ultimately, groups of event pairs are linked together forming clusters. Each cluster is relocated individually and a least-squares solution is used to produce relative locations within a particular cluster (Waldhauser and Ellsworth 2000). Traditionally, clusters are established by linking numerous event pairs within a reasonable distance of each other automatically as an initial step of the relocation in hypoDD. Our entire data set relocates as one cluster due to the close proximity of hypocenters in the NMSZ using this approach. Thus, we choose to identify clusters prior to relocation based on knowledge of fault plane orientations in the area. By relocating individual clusters, damping and weighting can be adjusted to complement each cluster. We assign six clusters to the area of densest seismicity based on natural breaks in hypocenter locations and previous knowledge of fault planes (Figure 2) (Pujol et al. 1997). The results for individual clusters are found to converge to a solution more quickly and with less damping and more retention of phase data than relocation results where all events are relocated in a single cluster.

Damping is used to stabilize the inversion. The degree of damping is assessed using the condition number (CND), which is the ratio of the largest to smallest eigenvalue of the solution (Waldhauser 2001). A stable relocation with appropriate damping should produce a CND between 40 and 80 (Waldhauser 2001). Table 2 lists information on each cluster including the

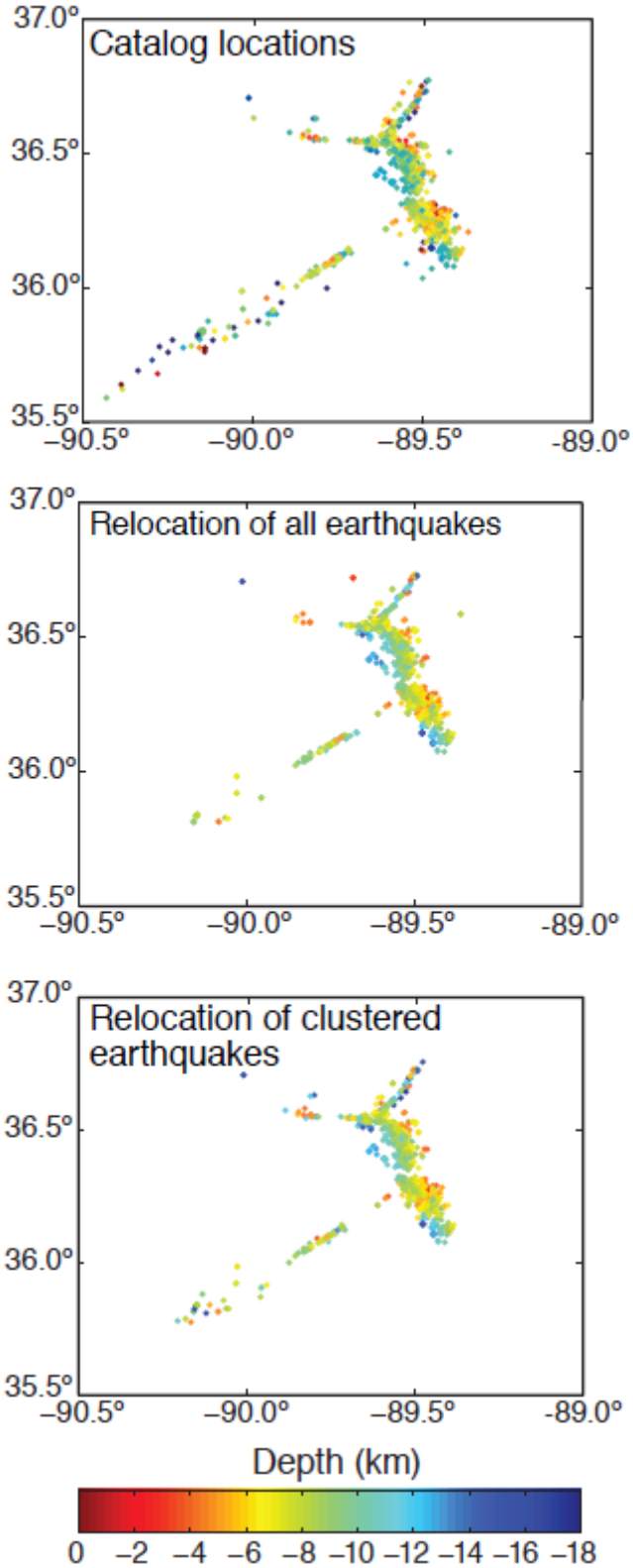

Figure 3. Comparison of locations and relocations of the NMSZ earthquake catalog. Top: Original locations. Middle: Relocations treating all earthquakes as one cluster. Bottom: Relocations of individual clusters.

number of events in the cluster, the number of events after relocation, the CND, and the damping value used. Earthquakes within individual clusters are relocated and the results are compared to original earthquake locations and to relocation of the entire data set as one cluster (Figure 3). Arguably, differential times cannot be used to refine absolute earthquake locations, but since the spatial differences between locations and relocations is small, this comparison is reasonable (Menke and Schaff 2004).

TABLE 2
Relocation Parameters and Results

Cluster	EQ before relocation	EQ after relocation	CND	Damping	Mean shift (m) *x*	*y*	*z*
1	56	53	63	25	153	185	493
2	56	34	58	30	69	151	328
3	77	76	72	40	203	152	381
4	47	42	72	40	290	853	667
5	286	272	79	75	153	147	319
6	313	295	71	80	145	155	198

RESULTS

Relocations obtained when the entire data set is considered to be one cluster differ from the relocations obtained in individual clusters. Relocation results for individual clusters produce small changes in original earthquake locations that tighten hypocenter distribution along fault segments. The original catalog locations are shown in comparison to the relocations for each of the six clusters in Figures 4, 5, and 6.

Clusters 1 and 2—Southwest Segment (CGF-BA)

Clusters 1 and 2 make up the southwestern arm of seismicity, shown in Figure 2. Figure 4 is a cross-section through clusters 1 and 2 oriented N40E, parallel to the trend of seismicity. All of the earthquakes in clusters 1 and 2 are projected onto the cross-section. We divided this area into two clusters based upon earthquake distribution; the northern section is tight and linear, while the southern section is sparse and spatially scattered. Events in cluster 1 occur between 5 and 15 km depth, and events in cluster 2 occur from 5 to 16 km depth. The catalog locations in cluster 1 appear to indicate a vertical fault. The relocations show a more defined vertical alignment of hypocenters. The mean shift of earthquakes in cluster 1 (cluster centroid) after relocation is shown in Table 2, with the x direction running east–west and the y direction running north-south.

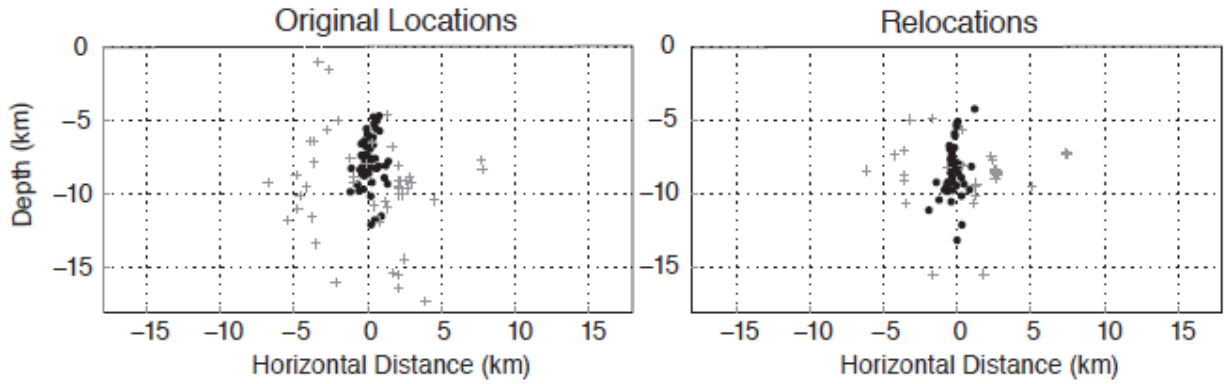

Figure 4. Original locations and relocations of clusters 1 and 2. Circles indicate earthquakes in cluster 1 and crosses indicate earthquakes in cluster 2. Cross-section is oriented N40E.

The original locations in cluster 2, as well as the relocations, show no distinct linear feature.

Cluster 3—Northwest Segment

Figure 5 (top) shows the locations and relocations in map view of cluster 3, the northwestern arm of seismicity. This arm is thought to be a left-lateral strike-slip fault based on focal mechanism solutions (Johnson 2008). Earthquakes in this cluster occur at depths of 2 to 18 km. The original locations form a cloud of seismicity trending east–west, and the fault plane is not clearly defined. The relocations collapse to delineate a sharper fault plane trending east–west, though some events continue to locate off-fault.

Cluster 4—Northeast Segment

Cluster 4 contains earthquakes associated with the northeastern arm of seismicity (Figure 2). Figure 5 (bottom) shows a cross-section oriented N25E, along the trend of seismicity. The original locations indicate a vertical fault, with seismicity occurring between 1 and 17 km. The shift in the cluster centroid after relocation is shown in Table 2. The relocated hypocenters also indicate a vertical fault in this area. Some hypocenters may be located deeper than 17 km. Shallow earthquakes, apparent in the original data, are probably not well recorded and are eliminated from our study because they do not meet parameter specifications.

Cluster 5—Northern Central Segment (RF)

The RF contains the majority of earthquakes in the NMSZ and is believed to be a reverse fault dipping to the southwest (Chiu et al. 1992; Johnston and Schweig 1996). We divide the fault into two clusters because this feature is often characterized as at least two independent arms of seismicity (Mueller and Pujol 2001). Cluster 5 is the portion of the RF north of the intersection of the CGF-BA fault. Relocations are shown in Figure 6 (top). Original earthquake locations and relocations occur between depths of 2 to 14 km. The fault is characterized by a shallow dip between 30 to 35 degrees. The relocations show a tightening in the earthquake distribution. In particular, the lower bound of the fault appears to be sharply defined.

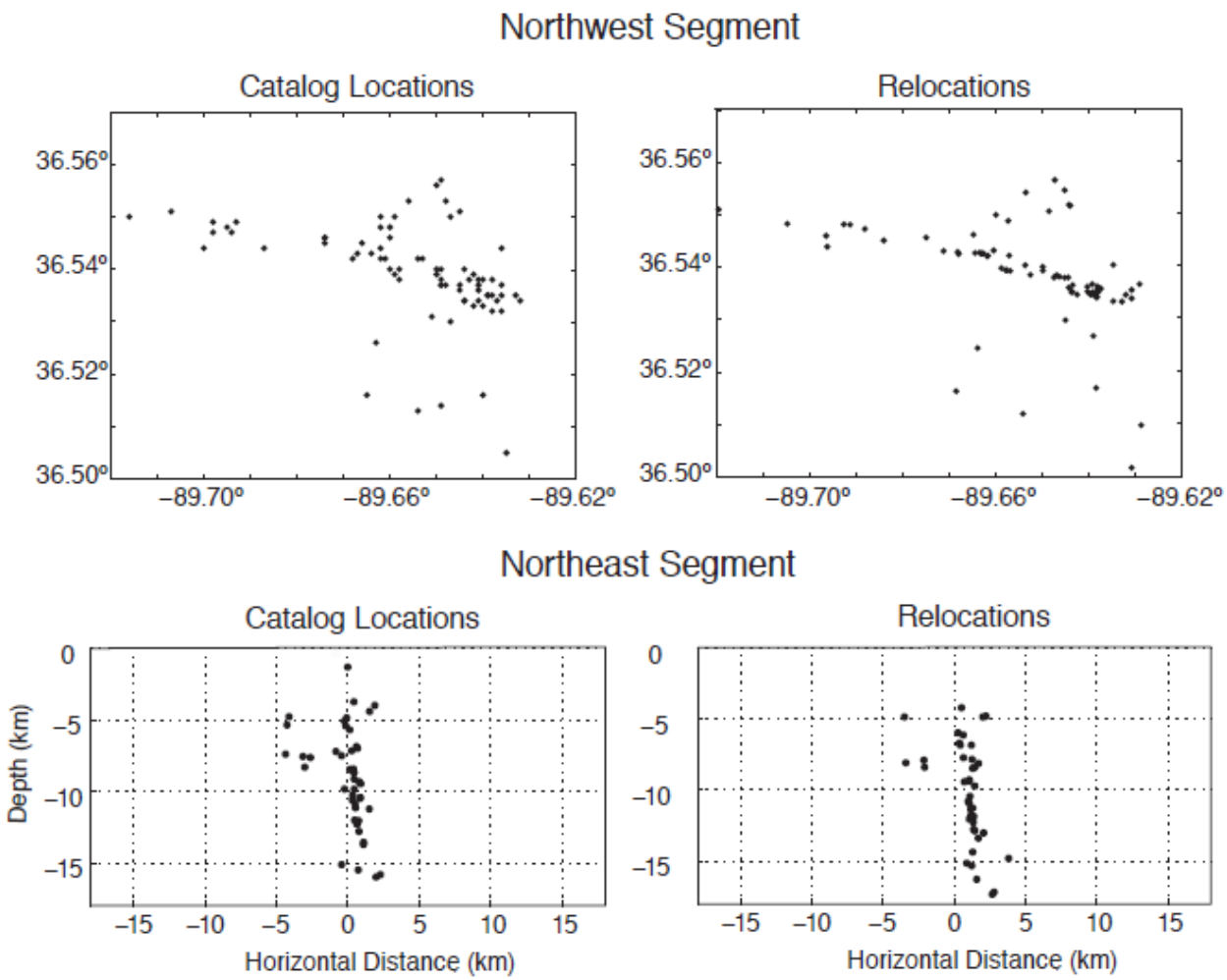

Figure 5. Original locations and relocations of clusters 3 and 4. Catalog locations on the left and relocations on the right. Top: Cluster 3 shown in map view. Bottom: Cluster 4 shown in cross-section oriented N33E.

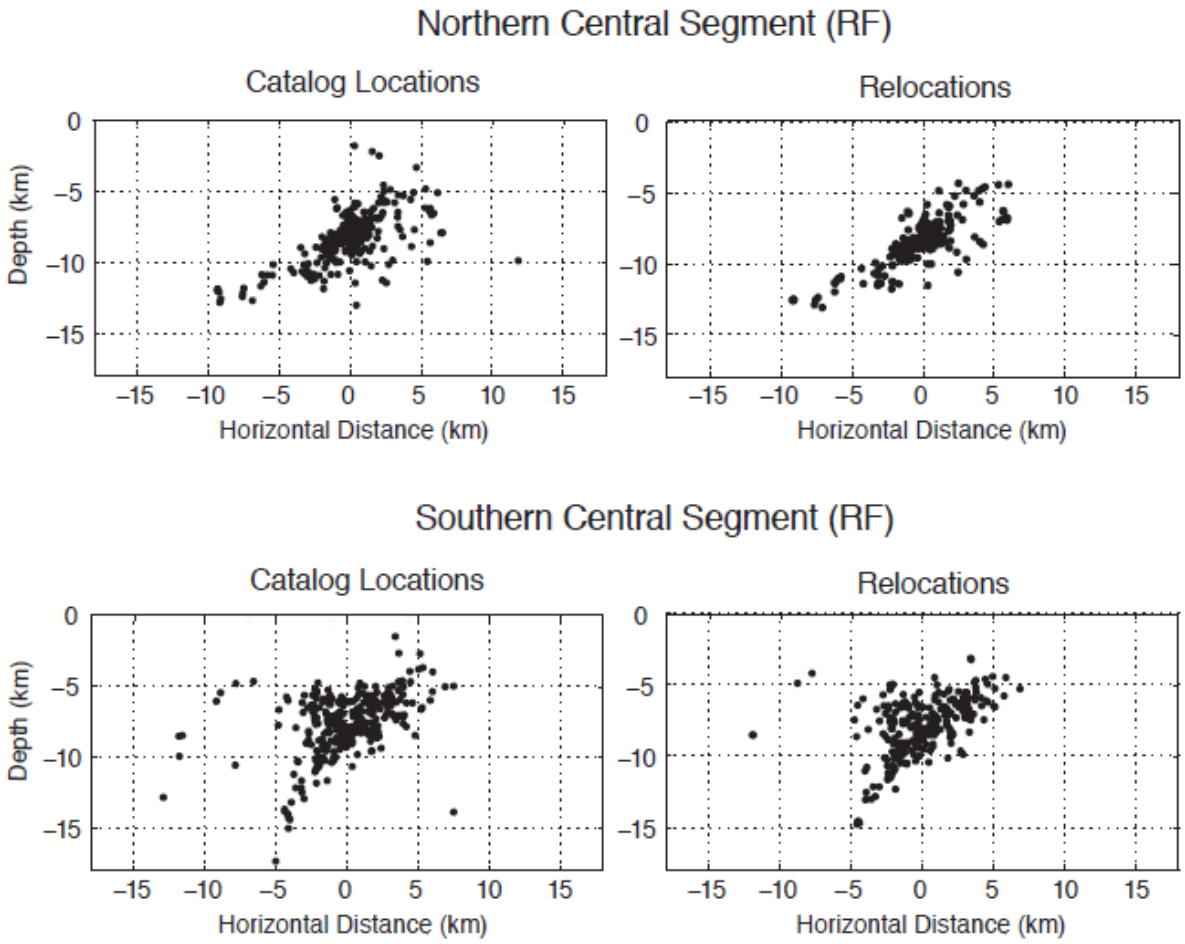

Figure 6. Original locations and relocations of clusters 5 and 6. Catalog locations on the left and relocations on the right. Top: Cluster 5 shown in cross-section oriented N18W. Bottom: Cluster 6 shown in cross-section oriented N33W.

Cluster 6—Southern Central Segment (RF)

Cluster 6, the largest cluster in the data set, represents the southern arm of the RF. Relocations are plotted in Figure 6 (bottom). Events in the cluster range in depth from 4 to 16 km after relocation. The relocations demonstrate a tightening of the event distribution and a slightly smaller dip on the fault plane; original catalog locations indicate a dip from 45 to 50° SW while the relocations suggest a dip of 40 to 45° SW. This section of the fault dips more steeply than the northern section, as has been found in previous studies using PANDA data (Chiu et al. 1992; Mueller and Pujol 2001). A comparison of the relocations for clusters 5 and 6 indicates the steeper dip on the southern end of the RF (Figure 6).

SUMMARY

The hypoDD relocations provide improved spatial constraints for most of the major NMSZ arms of seismicity relative to the initial catalog locations. This is illustrated most clearly in Figure 5, where cluster 3 condenses from a cloud of earthquake epicenters to a more linear feature, indicating a better-defined fault plane at the surface. Our study confirms many features found in previous studies using the temporary PANDA deployment (Pujol et al. 1997; Mueller and Pujol 2001). We image vertical, northeast-trending planes that are associated primarily with

right-lateral strike-slip mechanisms. We find that the dip on the RF changes at the intersection of the CGF-BA fault; the dip is 30–35° north of the intersection and steepens to 40–45° south of the intersection. This change in dip magnitude is supported by prior work (Mueller and Pujol 2001). The overall pattern of NMSZ seismicity does not change appreciably after earthquake relocation (Figure 3).

Relocation of earthquakes for the southwest arm of seismicity, the CGF-BA fault (Figure 4), tightens the earthquake distribution for the northern cluster but has minimal effect on the southern cluster. Relocated earthquakes in the northern cluster suggest a well-defined vertical fault plane, consistent with previous results (Mueller and Pujol 2001). In contrast with all other clusters, the earthquake location pattern in the southern CGF-BA cluster did not demonstrate meaningful change after relocation. Earthquakes in this cluster are sparse and many are not relocated. The sparse earthquake distribution could be insufficient to delineate the nature of the fault in this region. Another possibility is that the earthquakes do not occur on a single fault plane but on several different, minor faults associated with the Blytheville Arch.

Clusters 3 and 4 (Figure 5) represent the two northern arms of seismicity in the NMSZ (Figure 2). Cluster 3 contains events associated with the northwest arm, an E–W-trending fault with primarily left-lateral strike-slip motion. Several events did not relocate closer to the fault plane and the distributed earthquake pattern may be indicative of unidentified, minor faults, as in the case of cluster 2. Relocations for the northeastern segment (cluster 4), a right-lateral strike-slip fault, do not show major changes relative to the original locations. Several hypocenters in the original locations are relocated to greater depth, but not in a systematic way indicative of unmodeled velocity structure. One interesting point is that the original locations indicate a possible change in orientation at the base of the fault. The relative relocations do not demonstrate this; rather, the entire fault appears more vertical.

The RF is the most seismically active portion of the seismic zone (Figure 2). Catalog locations along the northern section (cluster 5, Figure 6) indicate a southwest-dipping fault with a dip of around 30 to 35 degrees. HypoDD relocations are consistent with this geometry but show a more sharply defined lower bound on the fault. A possible explanation for the sharper lower bound following relocation is that the trace of the fault is aligned along the lower bound of the relocations and the additional seismicity above the fault trace is within the hanging wall of the fault block. The southern part of the RF (cluster 6) has a steeper dip than the northern part (cluster 5), as can be seen in Figure 5. Different characteristics for the northern and southern parts of the RF are not surprising. The northern part has a simple structural interpretation; it is a compressive, left step-over fault between two right-lateral strike-slip faults (Russ 1982; Schweig and Ellis 1994; Odum et al. 1998). The presence of the southern part of the RF is enigmatic; there is no evidence that it is serving as a step-over fault, and its role in the seismotectonic framework of the NMSZ is not clear.

The close correspondence of the hypoDD relocations and the original catalog locations demonstrate the high quality of the permanent network data set. Continued recording of microseismicity by the network over time will allow better constraints to be placed on seismogenic structures associated with the major arms of seismicity. In particular, we may be able to better define faulting associated with the southern portion of the CGF-BA fault (cluster 2)

and the left-lateral northwestern fault (cluster 3). Earthquake relocations in conjunction with tomography will provide insights into the velocity heterogeneity associated with the complex RF fault system.

Part 2: Using Earthquake Focal Mechanisms to Investigate Seismotectonics in the New Madrid Seismic Zone

INTRODUCTION

The NMSZ is situated within the northern Mississippi Embayment. About 200 earthquakes per year are recorded here by the Cooperative New Madrid Seismic Network (CNMSN) with magnitudes that since 2000 range from 0.3 to 4.1 (Cooperative New Madrid Seismic Network, http://www.ceri.memphis.edu/seismic/). In 1811 and 1812 three large intraplate earthquakes (Magnitudes ~7-8) occurred near the town of New Madrid, MO, and they are estimated to be the largest intraplate earthquakes in the historic record (Johnston and Kanter, 1990). Paleoliquefaction studies show that very large earthquakes occurred in A.D. 900 ± 100 and A.D. 1450 ± 150 years, suggesting a pattern of repeating earthquakes with a return period around 500 years (Tuttle *t al.*, 2002). Given that the study area is ~2000 km from the nearest plate boundary, it is difficult to comprehend why large earthquakes occur in the NMSZ. Crustal deformation models have been created to provide a mechanism for earthquakes in NMSZ. Many models have been proposed (e.g. Forte *et al.*, 2007; Grana and Richardson, 1996; Grollimund and Zoback, 2001; Kenner and Segall, 2000; Liu and Zoback, 1997; Pollitz *et al.*, 2001), yet no model provides a widely accepted mechanism for earthquakes in intraplate regions. The development of a comprehensive, physical model for long term deformation in intraplate areas is hampered by a scarcity of data. One purpose of this study is to provide an estimate of the local stress variation(s) present in the crust to help constrain those models.

Figure 7 shows the locations for focal mechanisms generated in this study and the locations for historic events from past studies. Detailed information on the historic events is listed in Table 3. Focal mechanisms generated from this study that are located in the Central, North-Northwest trending, arm of seismicity are broken into 3 groups; a South Central Group, Mid-Central Group, and North Central Group. The other 3 groups are made up of focal mechanisms from the Southern Arm, Northern Arm, and Northwestern Arm.

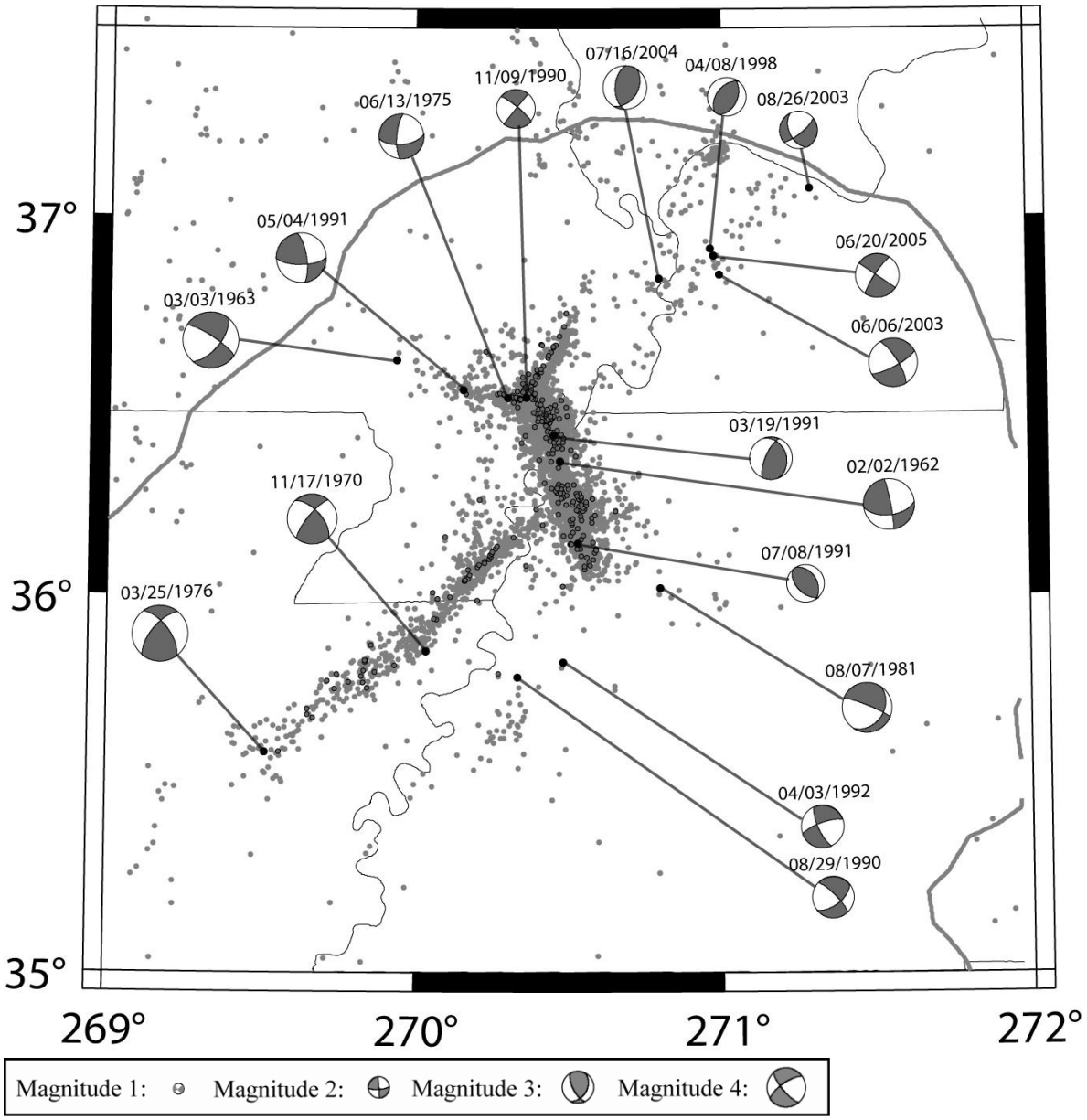

Figure 7 Map showing focal mechanisms from past studies. Refer to Table 1 for information on each one. The light gray circles are locations of historic seismicity from 1974 to 2007. Locations of earthquake focal mechanisms from this study are represented by the dark gray circles. The thick gray line is an outline of the Mississippi Embayment.

The Southern Arm extends from Marked Tree, AR northeast across the Mississippi River just west of Ridgely, TN. The South Central Group extends from just southeast of Gratio, TN northward to Ridgely, TN. The Mid-Central Group extends from Tiptonville, TN northward to an area located across the Mississippi River east of Point Pleasant, MO. The North Central Group extends from the eastern Kentucky-Tennessee border at the Mississippi River oxbow to New Madrid, MO. The Northern Arm extends from New Madrid, MO to East Prairie, MO. The Northwestern Arm extends from New Madrid, MO to Risco, MO.

Only a small number of focal mechanisms from the NMSZ are published in professional journals. Source parameters of those are listed in Table 3. Herrmann (1979) used P wave first

motions along with amplitude and phase data from long-period Love and Rayleigh waves to determine 22 focal mechanisms in Eastern North America. Only 9 of those occurred in the study area. They are consistent with right-lateral strike-slip motion on the Southern Arm, and left-lateral movement on the Northwestern Arm.

Table 3. Seventeen earthquakes from past studies in the NMSZ

Event	Lat.	Long.	Depth	Mag.	Strike	Dip	Rake	Author
02/02/62	36.37	-89.51	07.50	4.2	350	84	145	Herrmann (1979)
03/03/63	36.64	-90.05	15.00	4.6	304	78	-028	Herrmann & Ammon (1997)
11/17/70	35.86	-89.95	16.00	4.1	220	75	150	Herrmann (1979)
06/13/75	36.54	-89.68	09.00	3.7	085	60	-020	Herrmann (1979)
03/25/76	35.59	-90.48	12.00	4.6	220	65	150	Herrmann (1979)
08/07/81	36.03	-89.18	22.80	4.1	035	33	-166	C. Chiu(1997)
08/29/90	35.79	-89.65	14.73	3.4	053	60	-166	C. Chiu(1997)
11/09/90	36.54	-89.62	06.30	3.2	310	80	000	Z. Liu(1997)
03/19/91	36.44	-89.53	08.80	3.5	204	69	108	Z. Liu(1997)
05/04/91	36.56	-89.83	08.00	4.1	090	68	020	Herrmann & Ammon (1997)
07/08/91	36.15	-89.45	11.80	3.1	330	40	100	Z. Liu(1997)
04/03/92	35.83	-89.50	16.32	3.5	251	74	-163	C. Chiu(1997)
04/08/98	36.94	-89.01	07.80	3.2	025	45	080	Shumway (2008)
06/06/03	36.87	-88.98	02.60	4.0	329	75	-014	Horton (2005)
08/26/03	37.10	-88.68	01.90	3.1	052	75	-042	Shumway (2008)
07/16/04	36.86	-89.18	04.40	3.6	183	52	071	Shumway (2008)
06/20/05	36.92	-89.00	18.70	3.6	215	80	180	Shumway (2008)

Herrmann and Ammon (1997) discussed large earthquake events in the Embayment since 1962. Newly available high-resolution digital seismic recordings allowed them to improve estimates of source parameters for the smaller events. They compared revised results to earlier estimates and find that the high-resolution seismic data is helpful for constraining parameters of 2 previously published events. Chiu *et al.* (1997) investigated 75 earthquakes from 1974-1994 with magnitude ~0.1-4.0 occurring on the Southeastern Margin of the Reelfoot Rift. They determined 9 focal mechanisms, and concluded that right-lateral strike-slip and reverse slip are occurring on the southeastern margin of the Reelfoot rift. Shumway (2008) projected the length of the New Madrid North Fault (NMNF) northward based on the size of the 1811-1812 New Madrid events, and the microseismicity that defines the NMNF. She determined 19 events, half of which show a north-northeast trending nodal plane and right-lateral strike-slip. Liu, Z. (1997, SLU Dissertation), an unpublished dissertation, determined 54 focal mechanisms using PANDA data (Chiu *et al.*, 1992) that is located mainly in the Central Segment.

Focal mechanisms in the Central Segment of the NMSZ from this study show a complex pattern of fault plane orientations on an apparent thrust fault (Chiu *et al.*, 1992). The complexity of focal mechanism nodal planes in NMSZ is most likely caused by local rotations in the crustal stress (Street *et al.*, 1974). One of the primary motivations of this study is to increase the number of focal mechanisms using new data from the CNMSN. This study provides 194 focal mechanisms located in the Central Segment that can further our understanding of the faulting that occurs there.

Numerous rotations of the maximum horizontal compression (S_{Hmax}) orientation over time are partly responsible for complex structure of the strata underlying the Embayment and for the formation of the NMSZ. Currently, the S_{Hmax} direction for eastern North America is approximately 60° -65° (Zoback and Zoback, 1989). Estimations of local stress orientations using focal mechanisms vary according to location in the northern Mississippi Embayment. Currently, S_{Hmax} in NMSZ rotates to around 70° to 80° [e.g. 73°-84° (Ellis, 1994); 80° (Grana and Richardson, 1996)]. This study intends to delineate local patterns of crustal stress to help constrain models of crustal deformation.

A discussion given in the 'Focal Mechanism Maps' section of this paper compares focal types from the 6 regions of this study to the expected slip models. In the following section, a summary is given on the geology and the tectonic history followed by an introduction to the seismic data available for this study. This is followed by an explanation of the methods used for creating the focal mechanisms, and then, a discussion of focal mechanisms results. Then, I will explain a method for the stress inversion of focal mechanisms and give results of the stress inversions.

GEOLOGY OF THE STUDY AREA

The NMSZ is spatially associated with the Reelfoot rift, a geologic feature that was brought about by the lateral extension of Laurentia 750Ma due to the break-up of super-continent Rhodinia (Burke and Dewey, 1973). The stress field remained extensional through the middle Cambrian with the tension axis oriented approximately NW to SE (Dart and Swolfs, 1998). The rift is bound by two parallel, 300km long, normal displacement faults trending NE-SW, separated by a width of about 70 km. The Precambrian surface is displaced as much as 3 km on the northwestern bounding fault with nearly vertical dip to the southeast. Approximately 3 km of displacement is observable on the southeastern bounding fault with nearly vertical dip to the northwest.

Possible reactivation of the Reelfoot aulacogen occurred in the mid-Cretaceous and is attributed to the region passing over the Bermuda hotspot track (Cox and Van Arsdale, 2002; Morgan, 1983) during the disassembly of Pangea. Subsequent uplift of the region caused reactivation of basement faults, and a major marine regression that eroded ~2km of strata (Cox and Van Arsdale, 2002). This unconformity separates ~2km of Late Cambrian to Early Ordovician Knox (Arbuckle) from the Late Cretaceous. The stress field has remained, since the Cretaceous, with the compression axis oriented ENE to EW.

The northern Mississippi Embayment is composed of poorly consolidated to unconsolidated Late Cretaceous through Quaternary sediments that plunge to the southwest (Stearns, 1957). The

Embayment sediments thicken southward towards Memphis, and thin out laterally from the center of the Embayment to the east and to the west (Stearns, 1957). The Embayment sediments dip towards the south and towards the center of the trough, but the Paleozoic rocks below dip to the northeast north of the Pascola Arch and to the southwest south of the Pascola Arch (Ervin and McGinnis, 1975). The post-Paleozoic Embayment sediments overlying the Reelfoot rift range in thickness from 0 to ~1 km (Dart and Swolfs, 1998). Embayment thickness in the NMSZ is ~0.6 km (Kane *et al.*, 1981).

Geophysical studies suggest that the Reelfoot rift is underlain by a high velocity and high density rift pillow (Ginzburg *et al.*, 1983; Grana and Richardson, 1996; Mooney *et al.*, 1983). The location of the rift pillow is debated. Magmatic bodies in the Embayment are not uncommon. The change in elevation of the surface topography in this region is very modest, but the uplifts can be reproduced using long term deformation models (Gomberg and Ellis, 1994). Lake County Uplift is a broad uplift that contains Tiptonville Dome and Ridgely Ridge. At maximum, Tiptonville Dome is ~10m higher than the surrounding areas. Ridgely Ridge is at the southern tip of Lake County Uplift and is interpreted as a pre-1811 uplifted block (~6 m) that lies between parallel strike-slip faults (Odum *et al.*, 1998). Reelfoot scarp is about 8 m high (Van Arsdale *et al.*, 1995), and forms the boundary between the Tiptonville Dome and Reelfoot Lake.

METHOD

The CNMSN prior to 1998 was composed mostly of single component (vertical) short-period seismometers, and so it does not provide reliable S-wave arrival times (due to converted phases) and no S-wave polarity information. This is important because S-wave polarity can be used to help constrain focal mechanisms not already well-constrained by P-wave polarity. An upgrade of the network in 1998 included deployment of 96 three-component stations and the installation of 13 broadband seismometers. From 2000 through 2007, 1,491 events with magnitude >1.0 were recorded by the CNMSN in the Mississippi embayment.

Figure 8 shows the radial, transverse, and vertical components of a 2.2 magnitude earthquake recorded by the CNMSN at station LPAR on May 1, 2005 on the Southern Arm. The apparent first motion polarity of SV- and SH- waves shown in north-south and east-west components rarely correspond to first motion polarity given by the rotated radial and transverse components. Therefore, rotating the horizontal components of each event to radial and transverse is necessary in order to accurately interpret the polarity of the S-wave components. The P-S converted phase is observable on the radial component, and the S-P converted phase is observable on the vertical component. The SV- phase is not utilized in this study because rotating the two horizontal components causes interference on the radial component from the vertical component.

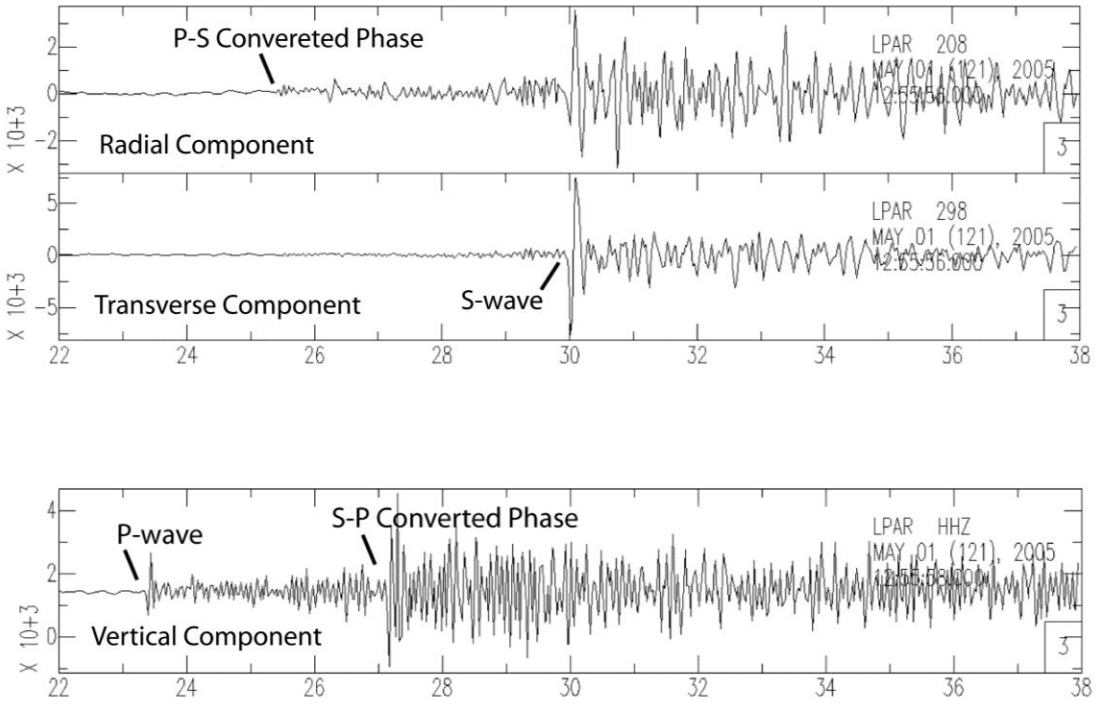

Figure 8. Illustration of waveforms showing typical body wave arrivals in the NMSZ

Determination of Focal Mechanisms

Two programs, FPFIT (Reasenberg and Oppenheimer, 1985) and FOCMEC (Snoke, 1984), are used to determine focal mechanisms because each one uses different types of seismic waves for determining focal mechanisms. Focal mechanisms are a representation of the radiation pattern of seismic waves due to an earthquake on a fault plane with a given orientation. The radiation pattern predicts the polarity of motion and the relative amplitude of seismic waves (e.g. P-, SH-, or SV- waves; P-waves can be up or down) determined by the orientation (strike, dip, and rake) of a double couple point source. The directions of the waves are given in angular coordinates relative to the seismic point source and earth's surface directions.

Equations for the P- and SH- radiation patterns are given by Eq. 4.89 and 4.91 of Aki and Richards (2002) which are shown below as equations (1.A) and (1.B):

$$P = \cos(\lambda) * \sin(\delta) * \sin^2(I_\zeta) * 2 * \sin(\varphi-\varphi_s) * \cos(\varphi-\varphi_s) - \cos(\lambda) * \cos(\delta) *$$

$$2 * \sin(I_\zeta) * \cos(I_\zeta) * \cos(\varphi-\varphi_s) + \sin(\lambda) * 2 * \sin(\delta) * \cos(\delta) * (\cos^2(I_\zeta) - \quad \textbf{(1.A)}$$

$$\sin^2(I_\zeta) * \sin^2(\varphi-\varphi_s)) + \sin(\lambda) * (\cos^2(\delta) - \sin^2(\delta)) * 2 * \sin(I_\zeta) * \cos(I_\zeta) * \sin(\varphi-\varphi_s)$$

$$SH = \cos(\lambda) * \cos(\delta) * \cos(I_\zeta) * \sin(\varphi-\varphi_s) + \cos(\lambda) * \sin(\delta) * \sin(I_\zeta) * (\cos^2(\varphi-\varphi_s) - \sin^2(\varphi-\varphi_s)) + \sin(\lambda) * (\cos^2(\delta) - \sin^2(\delta)) * \cos(I_\zeta) * \cos(\varphi-\varphi_s) - .5 * \sin(\lambda) * 2 * \sin(\delta) * \cos(\delta) * \sin(I_\zeta) * 2 * \cos(\varphi-\varphi_s) * \sin(\varphi-\varphi_s), \quad \textbf{(1.B)}$$

where I_ζ = incidence angle (from source point), φ = azimuth (station relative to north), φ_s = strike, δ = dip, and λ = rake of fault plane. The solutions for the P- or SH- radiation patterns range from -1 to +1. Polarities of the P- and SH-wave arrivals correspond to the sign of the solution. A range of acceptable fault orientations can be determined by comparing the observed radiation pattern of seismic waves with that predicted by the Aki and Richards equations.
The program FPFIT utilizes just P-wave polarity to constrain focal mechanisms. FPFIT iterates through all possible fault orientations comparing the observations to the predicted polarities. The best solution has the minimum misfit between the observations and predictions at all stations. Uncertainty of fault parameters is based on the value of misfit. A solution with < 20° uncertainty in all fault parameters is deemed well-constrained in this study.

The program FOCMEC utilizes SH-wave polarity in addition to P-wave polarity to constrain focal mechanisms. SH- arrival polarity is obtained by examination of the transverse component (Figure 8). The SH- arrival is more difficult to distinguish than the P-wave arrival for a number of reasons including the possibility of incorrect rotation azimuth and or SV-wave interference. FOCMEC was run after each successive SH- pick in order to check the validity of that pick. This process is repeated until all possible picks are obtained.

FOCMEC also iterates through all possible fault orientations comparing the observations to the predicted polarities. FOCMEC does not use a measure of misfit for polarity data, but simply returns solutions that have less than a prescribed number of misfits. In this study, any solutions containing polarity errors are not accepted. Still this commonly leaves a range of acceptable solutions. For this study I report the solution having the minimum deviation from the mean of all acceptable solutions. The uncertainty of each fault parameter is assumed the largest deviation of that parameter from the mean.

Typically, focal mechanisms are characterized by type. Table 4 classifies focal mechanisms by associating rake of slip on a fault to the corresponding fault type. The values of rake used in Table 4 are modified from a table by V. Cronin (2004). The values in Table 4 were modified, because in observing focal mechanism solutions with rake values bordering oblique slip or strike-slip, the focal type becomes ambiguous. It was decided that the modified values in Table 4 are a better representation of the focal mechanism data set of this study.

Focal mechanisms generated in this study are compared to a hypothetical fault model predicted by principles of rock mechanics and the currently oriented stress field. The currently oriented regional ENE stress field (Zoback and Zoback, 1989) should yield dextral slip on the Southern and Northern Arms of NMSZ. Sinistral slip is expected on the Northwestern Arm, and thrust faulting should occur on the Central Segment. Secondary features that occur in a strike-slip regime relative to principles of rock mechanics (Davison, 1994) are also considered as probable fault planes.

Past studies speculate that NMSZ is a strike-slip fault regime interconnected by a compressive left-stepover (e.g. Odum *et al.*, 1998; Russ, 1982; Schwieg and Ellis, 1994). If the NMSZ is a strike-slip fault regime, then it is reasonable to suggest that there are secondary features associated to the strike-slip faults. A hypothetical fault model was created with respect to

Andersonian faulting theory that says subsidiary features formed in unbroken rock are expected at certain orientations relative to the right-lateral master fault orientation and slip direction (Twiss and Moores, 2007). Any through going strike-slip faults that occur in NMSZ could have subsidiary features. The orientation of those subsidiary features are expected to be variable since the NMSZ has experienced many different stress regimes over time.

Table 4: Fault type classification based on the rake of slip

Rake Of Slip	Fault Type
0° or 180°	pure strike-slip
-20° to 20°	left-lateral strike-slip
-140° to 140°	right-lateral strike-slip
20° to 70°	reverse left-lateral oblique
90°	pure dip-slip reverse
70° to 110°	reverse
110° to 140°	reverse right-lateral oblique
-110° to -140°	normal right-lateral oblique
-90°	pure dip-slip normal
-70 to -110°	normal
-20° to -70°	normal left-lateral oblique

Secondary faulting is explained using Andersonian faulting theory (Anderson, 1905). Antithetic Riedel (R) shear fractures and synthetic P shear fractures are expected at orientations $20° < \theta < 45°$ to the master right-lateral strike-slip fault. Antithetic Riedel-prime (R^1) shears and synthetic X shears are expected at orientations $45° < \theta < 90°$ to the main fault. Secondary reverse and normal faults can also be expected in a strike-slip regime. Secondary reverse faults are expected to have strike at angles $\geq 135°$ to the master fault, measured in the same sense as the shear sense on the fault. The trend of secondary normal faults is expected to occur at ~45° to the master fault, perpendicular to the trend of the secondary reverse faults.

Stress Inversion Technique:

Bott (1959) proposes that slip on any fault plane occurs in the same direction as the maximum resolved shear stress. An appropriate geometric shear stress orientation must compliment a given slip direction. Numerous inverse methods exist that calculate stress from fault-slip data. Each

method attempts to find a stress tensor that minimizes the misfit between observed slip direction and modeled slip direction.

Gephart (1990) estimates best-fitting stresses using a stress inversion method. For this study, the program FMSI (Gephart, 1990) is used to calculate an approximate contributive stress tensor using focal mechanisms determined in this study combined with data from previous studies. FMSI computes only the ratio of the stress tensor components not the actual stress magnitudes of each component. The ratio of contributing stress components are given by the magnitude ratio:
$R \equiv (\sigma_2 - \sigma_1)/(\sigma_3 - \sigma_1). \quad (0 \leq R \leq 1)$ **(2)**

For equation 2, if R = 1, then it can be concluded that σ_2 and σ_3 have equal magnitudes. It also goes that if $0.5<R<1$, then σ_2 and σ_3 have similar magnitudes. If $0<R<0.5$, then σ_1 and σ_2 have similar magnitudes. If R = 0, then σ_1 and σ_2 are equal in magnitude.

RESULTS

This study generated 183 focal mechanisms using FPFIT and 107 focal mechanisms with FOCMEC. Ninety-four of these are located in the Central Segment. The Northern Arm contains 20 focal mechanisms and the Northwestern Arm contains 25. Fifty-one are located in the Southern Arm. Out of the 290 solutions, 127 are defined as strike-slip, 107 are reverse events, and 56 are normal.

SOUTHERN ARM

Figure 9 is a cross section of earthquakes that occurred through 2000-2007 in the Southern Arm. An inset map of the NMSZ showing focal mechanism locations from this study is located in the upper right corner of Figure 3. Two major structures exist in the Southern Arm that can be observed by the pattern of seismic activity; the Blytheville Fault Zone (BFZ) and the Blytheville Arch (BA). These two structures are characterized by a change in the trend of seismic activity in the northern half and southern half of the Southern Arm. A clustered set of earthquakes is observable in the upper half of the Southern Arm in the BFZ, whereas a more dispersive group comprises the lower half of the Southern Arm where the BA is located. The azimuth of the BFZ is about 45° and the azimuth of the BA is variable. Taken together a trend of about N50°E fits the seismicity. The cross-section in Figure 3 is at 45° to best show the tight, vertical structure of the BFZ.

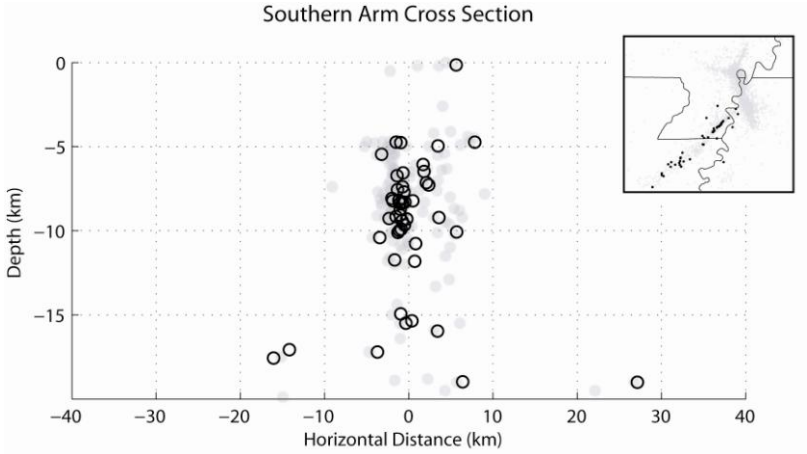

Figure 9. Cross section of focal mechanism locations from this study oriented at N45°E. Thick black circles represent focal mechanisms from this study and gray-filled circles show seismic activity from 2000-2007. For reference, the inset map shows seismic activity since 1974 as gray dots in the background, and focal mechanism locations in the Southern Arm as blue dots.

Focal mechanism locations in the upper half of the Southern Arm exhibit a linear trend matching the seismicity in map view. The earthquakes here illuminate a nearly vertical fault zone. These events make up the BFZ. They are dominantly right-lateral strike-slip on a near vertical fault. Focal mechanisms in the lower half of the Southern Arm also show right-lateral strike-slip on a nearly vertical nodal plane.

Fifteen focal mechanisms located in the Southern Arm are well-constrained FOCMEC solutions that utilize both P-wave and SH-wave first motion polarities. Half of the 36 strike-slip focal mechanisms in the Southern Arm show right-lateral motion on at least one nearly vertical (≥ 70°) nodal plane striking 45° ±20° (225° ±20°). Eight out of the 18 are located on the BA, and the other nine are located in BFZ. All but one of these 18 focal mechanisms is consistent with seismicity which illuminates the Southern Arm. Event ‘20060212’ is located on the Bootheel lineament, and it has a nodal plane that shows right-lateral slip on a vertical fault. At least one nodal plane for each strike-slip solution is consistent with secondary faults associated to a strike-slip regime (Davison, 1994; Twiss and Moores, 2007).

According to Andersonian faulting theory (Anderson, 1905), reverse faults subsidiary to a right lateral fault could occur on the Southern Arm within the strike ranges of 0° - 20° (180° - 220°). Seven out of ten reverse focal mechanisms in the Southern Arm show at least one nodal plane corresponding to that expected strike. The normal faults in the Southern Arm are expected to occur at ~90° or ~270° with dip <60°. All five normal focal mechanisms have at least one nodal plane which corresponds to or nearly fits that model. It is interesting that the orientation of the Central segment reverse fault is about 327°, nearly perpendicular to the Southern Arm and not within the range predicted by Andersonian mechanics.

CENTRAL SEGMENT

The Central Segment focal mechanisms are divided into a South Central group, a Mid-Central group, and a North Central group. Chiu *et al.* (1992) and Pujol *et al.* (1997) show cross sections that illustrate the South Central and North Central zones of seismicity dipping between 37ºSW

and 45ºSW. The reason for breaking the Central Segment into three parts is to allow for closer evaluation of the bend that separates the North Central region from the South Central region.

South Central Group:
Earthquakes in the South Central region illuminate a zone of seismicity that strikes ~327°. There are 40 reverse focal mechanisms in the South Central group. Approximately 17.5% of these have at least one nodal plane striking ~147° ±20° with dip < 60°. These focal mechanisms are compatible with the general trend of the Central Segment in the South Central region. A second family of nodal planes with strike 0º-45º (180º-225º) and dip ≤ 60º comprises 60% of the reverse faults. These 24 nodal planes could possibly be secondary to a through going strike-slip fault oriented parallel to the Southern Arm.

There are 34 strike-slip focal mechanisms in the South Central group. Four of those have an azimuth between 45°-65° (225°-245°). This is parallel to the orientation of the Southern Arm and Reelfoot Rift margins. There are 13 with at least one nodal plane striking 15º-35º (195°-215°), and near vertical dip (≥70º). This is parallel to the orientation of the Northern Arm and to the Northern Mississippi Embayment axis. Seismicity here shows a vertical linear trend located on the west side of the South Central Region, and could possibly be indicative of a through going strike-slip fault.

There are 13 normal focal mechanisms in the South Central group. Approximately 46% of the normal nodal planes has strike between 70º to 110º (250º to 290º) and dip ≤ 60º. These six focal mechanisms are possibly secondary features related to cross-cutting strike-slip faults parallel to the orientation of the Southern Arm. The other 38% have scattered nodal plane orientations. All normal events in Figure 4-7 occur at either end of the South Central Group.

Mid-Central Group

The Mid-Central group is located approximately where a bend in the seismicity of the Central Segment occurs. This bend connects the South Central Group to the North Central Group. Earthquakes here illuminate a fault zone that strikes at a slightly different angle than the North Central or South Central regions at about 18º. It is interesting that normal focal mechanisms make up the largest majority of focal types.

The Mid-Central group contains eight reverse focal mechanisms, 10 strike-slip focal mechanisms, and 12 normal focal mechanisms. One reverse focal mechanism strikes ~162° ±20° and has dip <60°. This orientation corresponds to the trend of Mid-Central seismicity. Four reverse focal mechanisms strike 0º-45º (183º-225º) with dip <60°. These could be reverse faults that are secondary to a through-going strike-slip fault that is oriented parallel to the Southern Arm. The other two focal mechanisms have strike ~340º. These two could be secondary reverse faults to a through-going strike-slip fault that is oriented parallel to the Northern Arm.
One out of the 10 strike-slip focal mechanisms is oriented 45°-65° (225°-245°) with dip >70º. This orientation is parallel to the Southern Arm and Reelfoot Rift margin. Four of the ten strike slip solutions have strike 15°-35° (195°-215°). Those four are parallel to the Northern Arm and Mississippi Embayment axis. Five out of the 12 normal events are oriented at ~95º or ~275º. These correspond to secondary normal faults related to a cross-cutting strike-slip fault oriented

parallel to the Southern Arm. Two of the other seven normal focal mechanisms have strike ~65º (245º). These could be normal faults that are secondary to a strike-slip fault oriented parallel to the Northern Arm.

North Central Group

Earthquakes in the North Central region illuminate a zone of seismicity that strikes ~147°. Figure 10 shows 36 reverse focal mechanisms in the North Central group. About 22% of the reverse focal mechanisms strike ~147° ±20° with dip < 60°. These eight are oriented parallel to the average trend of seismicity in the Central Segment. Reverse nodal planes that strike 170º-180º (320º -360º) could be related to a through-going strike-slip fault that is oriented parallel to the Northern Arm. Nodal planes with those orientations comprise ~33% of the reverse focal mechanisms. The other 16 reverse focal mechanisms have scattered nodal planes.

There are 19 strike-slip focal mechanisms from the North Central group. Seven of the 19 have strike 15º-35º (195º -215º). That orientation is parallel to the Northern Arm. Two have strike that is parallel to the Southern Arm (45º-65º or 225º-245º). The orientations of the other 10 strike-slip focal mechanisms correspond to secondary features. These features would be secondary to a through-going strike-slip fault that is oriented parallel to the Southern Arm.

The North Central group is comprised of 22 normal focal mechanisms. About 41% have nodal planes oriented at 90º (270º). Those nine could be secondary normal faults related to a strike-slip fault that is parallel to the Southern Arm.

NORTHERN ARM

The Northern Arm is comprised of a tightly clustered set of events that illuminate a nearly vertical fault oriented ~30°. Twelve out of 20 are strike-slip focal mechanisms. Half of the 12 strike-slip focal mechanisms show right-lateral strike-slip on a nearly vertical (≥ 70°) nodal plane striking ~30° ±20° (~210° ±20°). The other 6 strike-slip focal mechanisms have nodal planes that are consistent with various secondary faults that could be subsidiary to the Northern Arm.
Two out of the 7 reverse focal mechanisms have strike within 165°-190° (345°-10°). This is the range of strike for secondary features related to a strike-slip fault that is oriented parallel to the Northern Arm. The other five reverse focal mechanisms have scattered orientations. Secondary normal faults could occur at ~75° ±20° (~255°±20°). The single normal focal mechanism has a nodal plane that strikes 272° and dips 53°N. That orientation is compatible with a secondary feature for a strike-slip fault parallel to the Northern Arm.

NORTHWESTERN ARM

Earthquakes located within the Northwestern Arm illuminate a tightly clustered, nearly vertical fault oriented ~80°. There are 16 strike-slip focal mechanisms in the Northwestern Arm. Three of the 16 strike-slip focal mechanisms show left-lateral strike-slip on a nearly vertical (≥ 70°) nodal plane striking ~280° ±20° (~100° ±20°). These three focal mechanisms are consistent with seismicity which illuminates a vertical Northwestern Arm. The other 13 have a nodal plane that corresponds to secondary faults related to a strike-slip fault that is oriented parallel to the Northwestern Arm.

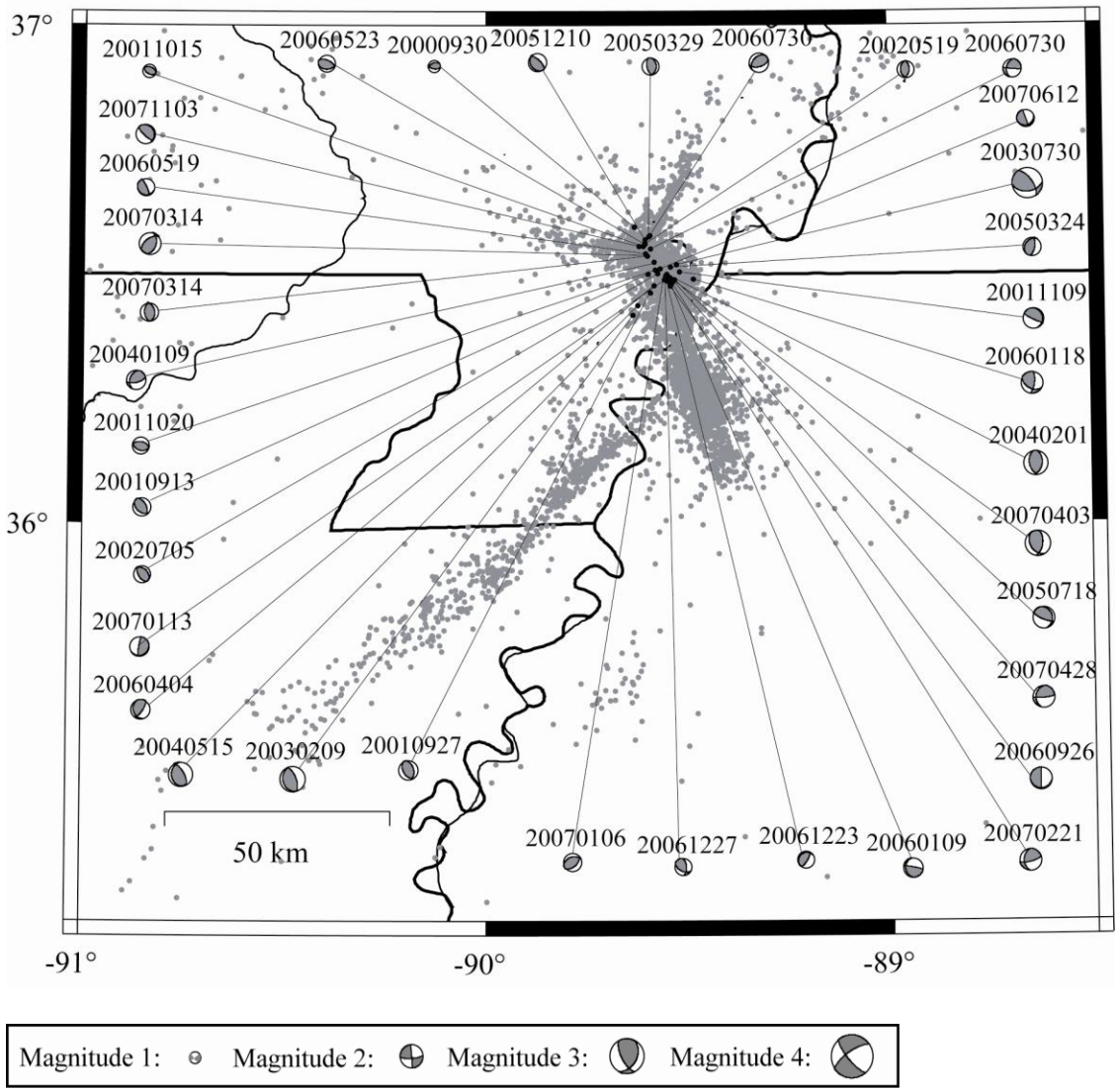

Figure 10. Map showing 19 reverse focal mechanisms from the North Central group of the Central segment. Size of each focal mechanism denotes the magnitude.

Reverse faults could occur within the strike ranges of 305°-325° (125°-145°). Five out of seven have that orientation with dip <60°. Normal faults could occur at ~35° (~215°). Neither of the normal focal mechanisms corresponds to that value.

DISCUSSION

Figure 11 is a matrix of rose diagrams of the strike-azimuth of individual focal mechanisms where strike-slip events are shown in the first column, reverse-slip in the second column and normal-slip events in the third. The top row is for the entire data set, the middle row for the southern segment, and the bottom row for the central segment. The Northern Arm and Northwestern Arm are not shown because they do not contain enough focal mechanisms to show any definite patterns. The nodal planes in each rose diagram are grouped into 10° bins. The

number of nodal planes within each bin is indicated by the numbers located on the right side of the diagram.

Observation of strike-slip events in the top row of Figure 5 reveals that there are at least two major trends of strike-slip faults in the NMSZ. One is oriented at about 50°. The other is oriented about 30°. The 50° trend also dominates the Southern Arm rose diagram where structures like the Reelfoot Rift boundary, the Blytheville Arch, and the Blytheville Fault Zone approximately parallel the Southern Arm of seismicity. The dominant trend in the Central Segment strike-slip rose diagram is 30°. This trend is parallel to the Mississippi Embayment axis and the Northern Arm of seismicity. All strike-slip rose diagrams also show a large trend at ~135° that are most likely auxiliary planes related to the previous trends although this trend roughly parallels the orientation of the Pascola Arch.

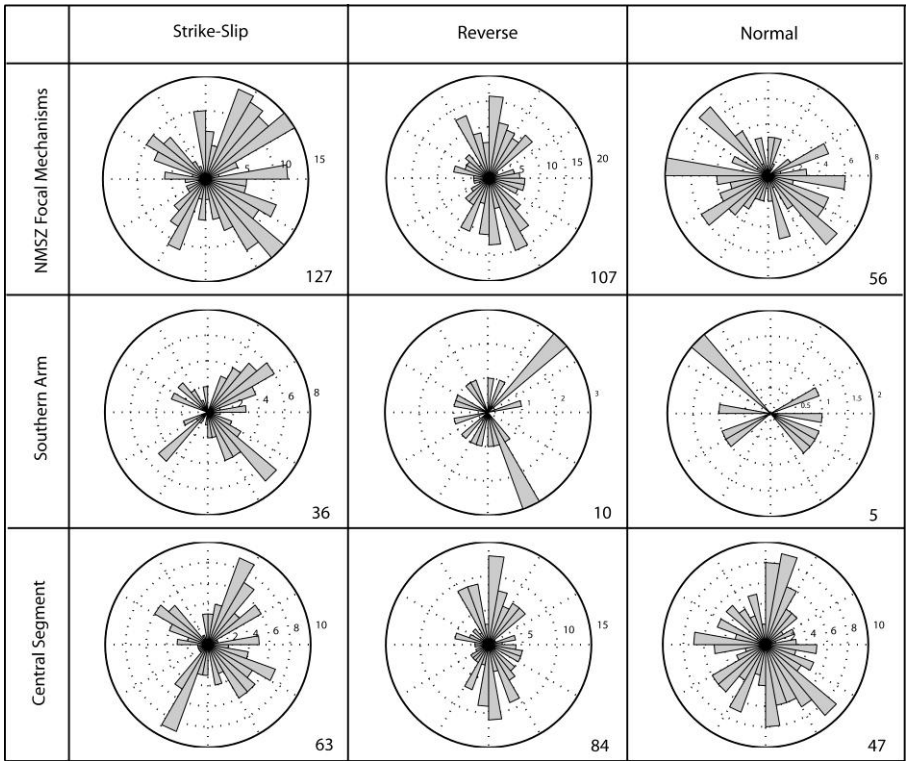

Figure 11. Consolidated table of focal mechanism solutions shown as rose diagrams. The gray bins are representative of nodal plane strike. The right-hand rule is used for designating strike direction and each diagram uses the same 360° scale like shown in the bottom-left box with all FOCMEC focal mechanisms plotted.

The reverse nodal planes for the NMSZ show 2 prominent N-S and NW-SE orientations with a smaller group oriented E-W. The nodal planes oriented N-S are in a direction favorable for a reverse fault that is secondary to a through-going strike-slip fault oriented 50°. That direction is parallel to the Southern Arm seismic trend, Reelfoot Rift boundary, Blytheville Arch, and Blytheville Fault Zone. The reverse nodal planes oriented 160° are in a direction favorable for a reverse fault that is secondary to a through-going strike-slip fault oriented 30°. That direction is parallel to the Mississippi Embayment axis and the Northern Arm seismic trend. The smaller E-W trend is most likely auxiliary planes.

Normal focal mechanisms in the NMSZ have scattered nodal planes. Out of the 56 normal focal mechanisms that occur in the NMSZ, 47 are located in the Central Segment. One group oriented at 135° could be secondary normal faults related to a strike-slip fault trending 50°. There is also an E-W trend of normal nodal planes that could be secondary to a strike-slip fault trending 50°. Another explanation for normal events in the Central Segment is that if the reverse fault were a blind thrust, extension is expected in the top of the hanging wall. The only real concentration of normal events in the hanging wall occurs in the Mid-Central Group. This is also the only location in the Central Segment where more normal events occur than any other focal type.

One method of estimating the regional stress orientation is to plot P and T axes from focal mechanisms. Compression axes of strike-slip focal mechanisms from this study are shown in Figure 12. Most of the compression axes show a NE to E trend. This agrees with results shown by Herrmann and Ammon (1997) for the March 3, 1963 and July 21, 1967 Missouri earthquakes and three events that occurred during 1990-1994. They find that the tension-axes of these are generally aligned N-S to NW-SE, while the compression-axes trend NE to E. Of course the orientation of the P-axis would only coincide with the orientation of the regional compressive axis if the faults were in previously unbroken rock.

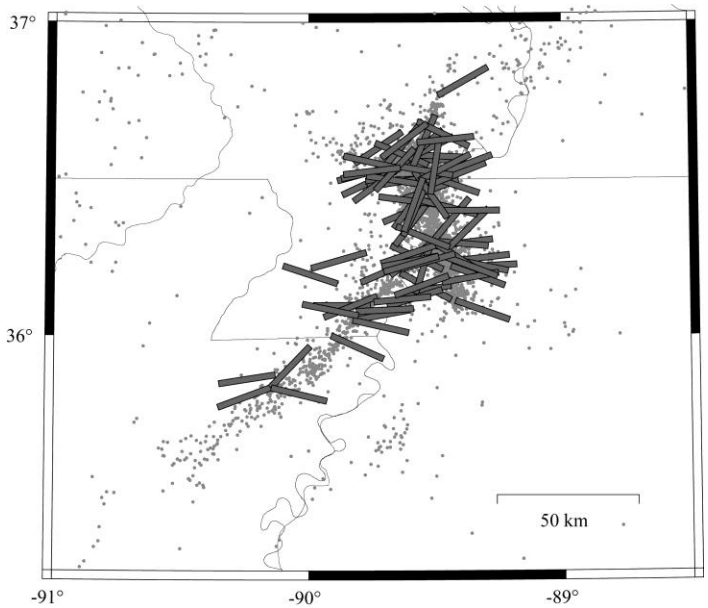

Figure 12. Map showing P-axis trend of all the strike-slip focal mechanisms in NSMZ

There are several methods for estimating the regional stress orientation from focal mechanisms. We use the method FMSI developed by Gephart (1990) discussed in the methods section. The stress tensor with a minimum measure of rotation between the observed fault orientation and stress model is plotted within a range of acceptable solutions within 95% confidence limits onto a composite focal sphere. The focal mechanisms are weighted where one well-constrained solution with minor uncertainty holds more weight than one with many solutions. Weights are ≥ 1 or ≤ 2 at an interval of 0.2.

Historic events are assigned a weight value of 1. Lower weighting is necessary because error estimates for the historic events are not known. These events are listed in Table 3. Results for the entire dataset including previously published focal mechanisms shows that the best fitting stress tensor has σ_1 oriented 79º with horizontal plunge, and σ_2 near vertical. The uncertainty in σ_1 is about 30 º, but the uncertainty in σ_2 is larger due to the even distribution of strike-slip and reverse events.

Stress inversion results of the focal mechanism P- and T- axes with respect to each of the 6 groups of focal mechanisms show local rotations of σ_1 in NMSZ. The Southern Arm shows σ_1 oriented at 70° for the southern half and 97° for the northern half. Orientation of σ_1 in the South Central Group and North Central Group is 88°. A rotation occurs in the Mid-Central group with σ_1 oriented 78°. The Northern Arm has σ_1 oriented at 70°, and the Northwestern Arm has σ_1 oriented at 62°. A common hypothesis that attempts to explain the local rotation of σ_1 is based on the influence that the Reelfoot rift pillow has on the surrounding crust.

Local rotations in the stress field of the NMSZ are attributed to the Reelfoot rift pillow (Grana and Richardson, 1996; Pollitz *et al.*, 2001). If the Reelfoot rift pillow is located at the lower boundary of the upper crust and mechanically connected to it, the downward force of the pillow in the lower crust would affect a small area of the upper crust. If it is completely segregated from the upper crust, strong fluid pressure gradients in the surrounding ductile lower crust could cause coupled downward forces to be exerted on the upper crust (Pollitz *et al.*, 2001).

CONCLUSIONS

There are two main trends of strike-slip nodal planes that match seismicity or structures in the northern Mississippi Embayment. There are ~50° oriented nodal planes that are parallel to the Southern Arm, Reelfoot Rift, Blytheville Arch, and Blytheville fault zone. And the ~30° oriented nodal planes are parallel to the Northern Arm and the Mississippi Embayment axis. Focal mechanism nodal planes that strike E-W correspond to the strike, dip, and slip expected for the Northwestern Arm, but no structures have that orientation in the Embayment.

There are two major trends of reverse faults in the Central Segment. One is oriented about 147° and is parallel to the average trend of seismicity in that segment. The other is oriented about 0°. This trend is anticipated for reverse faults secondary to through going strike-slip faults oriented about 45° such as the BFZ. Several studies have suggested the NMSZ is a strike-slip fault regime interconnected by a compressive left-stepover (e.g. Odum *et al.*, 1998; Russ, 1982; Schwieg and Ellis, 1994). The reverse faults in the Central segment oriented about 0° fit this suggestion well, but the ones oriented about 147° (along with the average trend of seismicity) do not fit well.

Normal faults in the NMSZ show a variety of nodal plane orientations. A small number show a NW-SE trend of normal nodal planes that could be secondary faults related to a 30° through-going strike-slip fault. Another trend oriented E-W could be secondary to a 50° through-going strike-slip fault. We investigated the possibility that normal faults reflect extension occurring in the hanging wall of the Reelfoot fault. Cross sections of the Central Segment reveal that the only concentration of normal events in the hanging wall occurs slightly in the Mid-Central Segment. All 3 groups of focal mechanisms in the Central Segment show focal types with complex spatial patterns.

This study shows that the overall orientation of σ_1 is 79°. This orientation is in agreement with past studies that estimate σ_1 is between 70°-80° (Ellis, 1994; Grana and Richardson, 1996). We further divided the results into 6 groups in order to estimate spatial variations of σ_1. The southern half of the Southern Arm, the Northern Arm, and the Northwestern Arm show orientations more comparable to stable North America (65°). Rotation occurs chiefly in the northern part of the Southern Arm and the Central segment. Grana and Richardson (1996) and Pollitz (2001) suggest rotation of σ_1 in the central NMSZ may be due to the proposed rift pillow, and that stresses from this structure have been influencing seismicity for over 100 m.y

REFERENCES

Aki, K., and P. G. Richards (2002). Quantitative Seismology, W. H. Freeman, 2nd edition.

Anderson, E. M. (1905). Dynamics of faulting: *Transactions Edinburgh Geological Society* **8**, 387-402.

Bickford, M., W. V. Schums, and I. Zietz (1986). Proterozoic history of the mid-continent region of North America. Geology 14, 492–496.

Burke, K., and J. F. Dewey (1973). Plume-generated triple junctions: key indicators in applying plate tectonics to old rocks, *Journal of Geology* **81**, 406-433.

Catchings, R. (1999). Regional Vp, Vs, Vp/Vs, and Poisson's ratios across earthquake source zones from Memphis, Tennessee, to St. Louis, Missouri. Bulletin of the Seismological Society of America 89, 1,591– 1,605.

Chiu, J. M., A. C. Johnston, and Y. T. Yang (1992). Imaging the active faults of the central New Madrid seismic zone using PANDA array data. Seismological Research Letters 63, 375–393.

Chiu, S. C., J. M. Chiu, and A. C. Johnston (1997). Seismicity of the Southeastern Margin of Reelfoot Rift, Central United States, *Seismological Research Letters* **68**, no. 5, 785–796.f

Cox, R. T., and R. B. Van Arsdale (2002). The Mississippi Embayment, North America: A first order continental structure generated by the Cretaceous superplume mantle event, *Journal of Geodynamics* **34**, 163-176.

Cronin, V. (2004). A Draft Primer on Focal Mechanism Solutions for Geologists, Baylor University, Retrieved from the World Wide Web: http://serc.carleton.edu/files/NAGTWorkshops/structure04/Focal_mechanism_primer.pdf, (January, 2007).

Csontos, R., and R. VanArsdale (2008). New Madrid seismic zone fault geometry. Geosphere 4, 802–813.

Dart, R. L., and H. S. Swolfs (1998). Contour mapping of relic structures in the Precambrian basement of the Reelfoot rift, North American midcontinent, *Tectonics* **17**, no. 2, 235-29.

Davison, I. (1994). Linked fault systems; extensional, strike-slip and contractional, in *Continental Deformation*, P.L. Hancock (Editor), pp. 121-142, Pergamon Press, New York, NY.

Dunn, M, S. Horton, H. DeShon, and C. Powell, High-resolution Earthquake Location in the New Madrid Seismic Zone, Fall AGU (2007).

Dunn, M, S. Horton, H. DeShon, and C. Powell, HypoDD Relocation of Earthquakes in the New Madrid Seismic Zone, eastern section of the Seis. Soc. Am., (2007).

Dunn, M, S. Horton, H. DeShon, and C. Powell, High Resolution Earthquake Location in the New Madrid Seismic Zone, Seismological Research Letters, v. 81 no.2, 406-413, 2010.

Ellis, W. (1994). Summary and Discussion of Crustal Stress Data in the Region of the New Madrid Seismic Zone. USGS Open File Report 1538.

Ervin, C. P., and L. D. McGinnis (1975). Reelfoot rift: Reactivated precursor to the Mississippi embayment. Bulletin of the Geological Society of America 86, 1,287–1,295.

Forte, A., J. Mitrovica, N. Simmons, and S. Grand (2007). Descent of the ancient Farallon slab drives localized mantle below below the New Madrid seismic zone. Geophysical Research Letters 34; doi:10.1029/2006GL027895.

Gephart, J. W. (1990). Stress and the direction of slip on fault planes, *Tectonics* **9**, no. 4, 845-858.

Gephart, J. W. (1990). FMSI: a FORTRAN program for inverting fault/slikenslide and earthquake focal mechanism data to obtain the regional stress tensor, *Computers and Geosciences* **89**, 9305-9320.

Ginzberg, A., W. D. Mooney, A. W. Walter, W. J. Lutter, and J. H. Healy (1983). Deep structure of northern Mississippi embayment, *American Association of Petroleum Geologists Bulletin* **67**, 2031-2046.

Gomberg, J. S., and M. A. Ellis (1994). Topography and tectonics of the central New Madrid Seismic Zone: Results of numerical experiments using a three-dimensional boundary-element program: *Journal of Geophysical Research* **99**, 20299-20310.

Grana, J., and R. Richardson (1996). Tectonic stress within the New Madrid seismic zone. Journal of Geophysical Research 101, 5,445– 5,458.

Grollimund, B., and M. D. Zoback (2001). Did deglaciation trigger intraplate seismicity in the New Madrid seismic zone? *Geology* **29**, 175-178.

Hamilton, R. M., and F. A. McKeown (1988). Structure of the Blytheville arch in the New Madrid seismic zone, *Seismological Research Letters* **59**, 117-121.

Hermann, R. B. (1979). Surface wave focal mechanisms for eastern North America with tectonic implications, *Journal of Geophysical Research* **84**, 3542-3552.

Herrmann, R. B., and C. J. Ammon (1997). Faulting parameters of earthquakes in the New Madrid, Missouri Region, *Engineering Geology* **46**, 299-311.

Hildenbrand, T. G., M. F. Kane, and W. Stauder (1977). Magnetic and gravity anomalies In the northern Mississippi Embayment and their spatial relation to seismicity: *U.S. Geological Survey Miscellaneous Field Studies*, Map MF-914, scale 1:1,000,000.

Hildenbrand, T., and J. Hendricks (1995). Geophysical Setting of the Reelfoot Rift and Relations between Rift Structures and the New Madrid Seismic Zone. USGS Professional Paper 1583.

Horton, S., W.-Y. Kim, and M. Withers (2005). The 6 June 2003 Bardwell, Kentucky, earthquake sequence: Evidence for the locally perturbed stress field in the Mississippi embayment. Bulletin of the Seismological Society of America 95, 431–453.

Horton, S.P. and G. Johnson, Earthquake Focal Mechanisms and Stress Estimates in the New Madrid Seismic Zone, SSA Annual Meeting (2010).

Howe, J. R. (1985). Tectonics, sedimentation, and hydrocarbon potential of the Reelfoot Aulocogen, *M.S. Thesis*, University of Oklahoma, Norman, 109 p.

Howe, J. R., and T. L. Thompson (1984). Tectonics, sedimentation, and hydrocarbon potential of the Reelfoot rift. Oil & Gas Journal 82, 179–190.

Johnson, G. (2008). Using earthquake focal mechanisms to investigate seismotectonics in New Madrid seismic zone. Master's thesis, University of Memphis.

Johnson G., S. Horton, M. Withers and R. Cox, Earthquake Focal Mechanisms from the New Madrid Seismic Zone, 2008 Annual Meeting, Santa Fe, New Mexico (2008).
Johnston, A. C., and E. S. Schweig (1996). The enigma of the New Madrid earthquakes of 1811–1812. Annual Review of the Earth and Planetary Sciences 24, 339–384.
Johnston, A. C., and L. Kanter (1990). Earthquakes in stable continental crust, *Scientific American* **262**, no. 3, 68-75.
Kane, M. F., T. G. Hildenbrand, and J.D. Hendricks (1981). Model for the tectonic evolution of the Mississippi embayment and its contemporary seismicity, *Geology* **9**, 563-568.
Kenner, S., and P. Segall (2000). A mechanical model for intraplate earthquakes: Application to the New Madrid seismic zone, *Journal of Geophysical Research* **101**, 6151-6170.
Lahr, J. C. (1980). HYPOELLIPSE/MULTICS, A Computer Program for Determining Local Earthquake Hypocentral Parameters, Magnitude, and First Motion Patterns. USGS Open File Report 59, 59-80.
Langenheim, V. E., and T. G. Hildenbrand (1997). Commerce geophysical lineament: Its source, geometry, and relation to the Reelfoot rift and New Madrid seismic zone, *Geological Society of America Bulletin* **109**, no. 5, 580-595.
Liu, L., and Y. Li (2001). Identification of liquefaction and deformation features using ground penetrating radar in the New Madrid seismic zone, USA, *Journal of Applied Geophysics* **47**, 199-215.
Liu, L., M. Zoback, and P. Segall (1992). Rapid intraplate strain accumulation in the New Madrid seismic zone. Science 257, 1,666–1,669.
Liu, L., and M. D. Zoback (1997). Lithospheric strength and intraplate seismicity in the New Madrid Seismic Zone, *Tectonophysics* **16**, 585-595.
Menke, W., and D. Schaff (2004). Absolute earthquake locations with differential data. Bulletin of the Seismological Society of America 94, 2,254–2,264.
Mooney, W., M. Andrews, A. Ginzburg, D. Peters, and R. Hamilton (1983). Crustal structure of the northern Mississippi embayment and a comparison with other continental rift zones. Tectonophysics 94, 327–348.
Morgan, W. J. (1983). Hotspot tracks and the early rifting of the Atlantic. *Tectonophysics* **94**, 123-139.
Mueller, K., and J. Pujol (2001). Three-dimensional geometry of the Reelfoot blind thrust: Implications for moment release and earthquake magnitude in the New Madrid seismic zone. Bulletin of the Seismological Society of America 91, 1,563–1,573.
Nelson, K., and J. Zhang (1991). A COCORP deep reflection profile across the buried Reelfoot rift, south-central United States. Tectonophysics 197, 271–293.
Odum, J. K., W. J. Stephenson, K. M. Shedlock, and T. L. Pratt (1998). Near-surface structural model for deformation associated with the February 7, 1812, New Madrid, Missouri, earthquake. Geological Society of America 110, 149–162.
Parrish, S., and R. VanArsdale (2004). Faulting along the southeastern margin of the Reelfoot rift in northwestern Tennessee revealed in deep seismic reflection profiles. Seismological Research Letters 75, 782–791.
Pollitz, F., L. Kellogg, and R. Burgmann (2001). Sinking mafic body in a reactivated lower crust: A mechanism for stress concentration at the New Madrid seismic zone. Bulletin of the Seismological Society of America 91, 1,882–1,897.
Pujol, J., A. Johnston, J. Chiu, and Y. Yang (1997). Refinement of thrust faulting models for the Central New Madrid seismic zone. Engineering Geology 46, 281–298.

Reasenberg, P. A., and D. Oppenheimer (1985). FPFIT, FPPLOT, and FPPAGE: FORTRAN computer programs for calculating and displaying earthquake fault-plane solutions, *U.S. Geological Survey Open-File Report* 85-739.

Russ, D.P. (1982). Style and significance of surface deformation in the vicinity of the New Madrid, Missouri, in McKeown, F.A. and Pakiser, L.C., eds., Investigations of the New Madrid, Missouri, Earthquake Region, USGS Professional Paper 1236-H, 95–114

Schweig, E. S., and M. A. Ellis (1994). Reconciling short recurrence intervals with minor deformation in the New Madrid seismic zone. Science 264, 1,308–1,309.

Schweig E. S. III, and Marple R T. (1991). The Bootheel lineament: A possible coseismic fault of the great New Madrid earthquakes, *Geology* **19**, 1025-1028.

Shedlock, K. M., and S. T. Harding (1982). Mississippi River seismic survey, *Geophysical Research Letters* **9**, 1275-1278.

Shumway, A. M. (2008). Focal Mechanisms in the Northeast New Madrid Seismic Zone, *Seismological Research Letters* **79**, no. 3, 469-477.

Snoke, J. A., J. W. Munsey, A. C. Teague, and G. A. Bollinger (1984). A program for focal mechanism determination by combined use of polarity and SV -P amplitude ratio data, *Earthquake Notes* **55**, no. 3, 15.

Stearns, R. G. (1957). Cretaceous, Paleocene, and lower Eocene history of the northern Mississippi Embayment, *Geological Society of America Bulletin* **68**, 1077-1100.

Street, R. L., R. B. Herrmann, and O.W. Nuttli (1974). Earthquake mechanics in the Central United States, *Science* **184**, no. 4143, 1285-1287.

Thomas, W. A. (1985). The Appalachian-Ouachita connection: Paleozoic orogenic belt at the southern margin of North America, *Annual Review of Earth and Planetary Sciences* **13**, 175-199.

Tuttle, M. P., E. S. Schweig, J. D. Sims, R. H. Lafferty, L. W. Wolf, and M. L. Hayn**es** (2002)**.** The earthquake potential of the New Madrid seismic zone, *Bulletin of the Seismological Society of America* **92**, no. 6, 2080-2089.

Waldhauser, F. (2001). HypoDD: A Computer Program to Compute Double-difference Hypocenter Locations. USGS Open File Report 25, 1–113.

Waldhauser, F., and W. L. Ellsworth (2000). A double-difference earthquake location algorithm: Method and application to the northern Hayward fault, California. Bulletin of the Seismological Society of America 90, 1,353–1,368.